JACS
JOURNAL OF THE AMERICAN CHEMICAL SOCIETY
Article
pubs.acs.org/JACS

# Enhanced Photoelectrochemical Performance of Cuprous Oxide/Graphene Nanohybrids

Egon Kecsenovity,[†,‡] Balázs Endrődi,[†,‡] Péter S. Tóth,[§] Yuqin Zou,[§] Robert A. W. Dryfe,[§] Krishnan Rajeshwar,[∥] and Csaba Janáky*[,†,‡]

[†]MTA-SZTE "Lendület" Photoelectrochemistry Research Group, Rerrich Square 1, Szeged H-6720, Hungary
[‡]Department of Physical Chemistry and Materials Science, University of Szeged, Rerrich Square 1, Szeged H-6720, Hungary
[§]School of Chemistry, University of Manchester, Oxford Road, Manchester M13 9PL, United Kingdom
[∥]Department of Chemistry and Biochemistry, The University of Texas at Arlington, Arlington, Texas 76019, United States

Supporting Information

**ABSTRACT:** Combination of an oxide semiconductor with a highly conductive nanocarbon framework (such as graphene or carbon nanotubes) is an attractive avenue to assemble efficient photoelectrodes for solar fuel generation. To fully exploit the possible synergies of the hybrid formation, however, precise knowledge of these systems is required to allow rational design and morphological engineering. In this paper, we present the controlled electrochemical deposition of nanocrystalline p-$Cu_2O$ on the surface of different graphene substrates. The developed synthetic protocol allowed tuning of the morphological features of the hybrids as deduced from electron microscopy. (Photo)electrochemical measurements (including photovoltammetry, electrochemical impedance spectroscopy, photocurrent transient analysis) demonstrated better performance for the 2D graphene containing photoelectrodes, compared to the bare $Cu_2O$ films, the enhanced performance being rooted in suppressed charge carrier recombination. To elucidate the precise role of graphene, comparative studies were performed with carbon nanotube (CNT) films and 3D graphene foams. These studies revealed, after allowing for the effect of increased surface area, that the 3D graphene substrate outperformed the other two nanocarbons. Its interconnected structure facilitated effective charge separation and transport, leading to better harvesting of the generated photoelectrons. These hybrid assemblies are shown to be potentially attractive candidates in photoelectrochemical energy conversion schemes, namely $CO_2$ reduction.

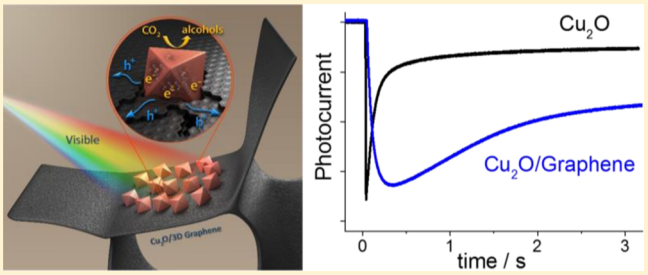


## INTRODUCTION

The increasing demand for efficient technologies to harvest the energy of the Sun is a major current driver of materials chemistry.[1] In addition to batteries and supercapacitors,[2] chemical fuels[3,4] (such as $H_2$ or methanol) are an attractive option for energy storage, especially given the intermittent nature of renewable sources. Photoelectrochemistry, which relies on chemical reactions initiated at the semiconductor/electrolyte interface[5] by photogenerated charge carriers, offers a viable avenue for the direct generation of solar fuels. Photoelectrochemical (PEC) water splitting, on an irradiated $TiO_2$ surface is the pioneering example,[6] and the field has grown rapidly during the past decades since the first discovery in the late 1960s.[5] On the other hand, $CO_2$ conversion is specifically challenging, because this reaction is multielectron in nature (e.g., 8 $e^-$ to $CH_4$) and thus requires long-lived charge carriers[7] and good electrocatalysts to obtain the targeted reduction product(s).[8,9] While several materials were tested in this vein, ranging from elemental semiconductors (e.g., p-Si)[10] to the most frequently studied oxides (mainly Cu-based binary and ternary oxides: e.g., $Cu_2O$,[11,12] $CuFeO_2$,[13−15] $CuBi_2O_4$,[16] and $CuNb_2O_6$[17]), to other compound semiconductors (e.g., GaP, CdTe, InP, GaAs, GaP, $FeS_2$, ZnTe),[5,18−23] none have reached the performance level required for practical utilization.

Considering the very complex requirements that have to be met by a photoelectrode (good light absorption, efficient charge carrier transport, rapid charge transfer kinetics, stability, etc.), it is not too surprising that no single "magic bullet" material has emerged so far.[5,24] Consequently, there are ample arguments in favor of assembling and studying intricate architectures with components that have precisely defined functionality and complementarity. There is literature precedence for composite materials outperforming their singular counterparts in PEC applications.[25,26] In particular, by providing a highly conductive scaffold, carbon nanotube and graphene-based composite materials are particularly attractive for photocatalytic[27,28] and PEC[29−31] applications in that they facilitate exciton dissociation and charge carrier transport.[32] Coherent, interconnected structures have additional benefits, rooted in the lack of carbon/carbon interfaces.[33−37]

**Received:** February 21, 2017
**Published:** May 1, 2017




DOI: 10.1021/jacs.7b01820
J. Am. Chem. Soc. 2017, 139, 6682−6692

As further, specific examples, enhanced anodic photocurrents were registered in a bioinspired ZnO/graphene assembly, where ZnO nanowires were obtained on honeycomb reduced graphene oxide (rGO).[38] Similarly, efficient charge transfer and suppressed electron−hole recombination was reported for a $Cu_2O$/rGO system.[39] Liquid phase exfoliated (LPE) graphene nanoplatelets were combined with $TiO_2$ nanoparticles, and improved photocatalytic efficiency was found for both $CH_3CHO$ oxidation and $CO_2$ reduction.[40] As yet another example, $BiVO_4$/rGO hybrids were employed in PEC water oxidation, and showed 10-times higher anodic photocurrent, compared to $BiVO_4$ alone.[41] Similar to the other cases reported, the enhanced activity was rationalized by the instantaneous electron injection to the rGO component from the photoexcited $BiVO_4$. The example of $Fe_2O_3$/rGO was used to demonstrate the different time scale of the various processes involved in a PEC reaction.[30] Most recently, we demonstrated how ultralong carbon nanotubes could be used as a scaffold for $Cu_2O$ nanocrystals to boost the PEC conversion of $CO_2$ to alcohols and formic acid.[42] Finally, the combination of carbon nanotubes (CNTs) and graphene can also be employed as conductive platforms, as demonstrated for a hematite ($Fe_2O_3$) containing composite, which was successfully employed for PEC water oxidation.[43] Notably, the reverse strategy was also demonstrated, where a carbon coating on the semiconductor surface acted both as stabilizer and cocatalyst.[44−46]

Despite the promising examples above, there is still much to be done to completely understand the effect of the nanocarbon scaffold, and thus to efficiently harness the synergy of the components in the hybrid configurations. Interestingly, there are many examples in the literature for photodriven (sometimes also referred as photocatalytic) reduction of $CO_2$ using suspensions of $Cu_2O$/nanocarbon hybrids,[47−49] but only a very few for the corresponding PEC scenario. In our opinion, this trend is rooted in the increased complexity of this latter configuration, where the most important two bottlenecks are (i) the lack of precise control over the composition and morphology in the hybrid architectures, which may deleteriously affect the PEC properties; and (ii) the lack of high quality nanocarbon electrodes with organized, interconnected three-dimensional (3D) structure. Consequently, there are only a few examples in the literature where 3D graphene nanostructures (such as foams) were used as a scaffold for different inorganic oxides. Nanorods of ZnO were hydrothermally deposited on a chemical vapor deposition (CVD)-grown 3D graphene foam and tested as electrochemical sensors.[50] Nanosheets of $Ni(OH)_2$ were hydrothermally grown on 3D graphene, and the hybrid was employed for the electrochemical sensing of glucose.[51] Finally, a mesoporous $Co_3O_4$ nanosheet array was deposited on a graphene foam to obtain high performance charge storage materials.[52] Importantly, none of these studies focused on the PEC performance of these nanocomposites.

Electrochemistry is a particularly versatile tool for the controlled synthesis of different semiconductors on nanostructured carbon surfaces. As shown in our recent Minireview article[26] it is possible to tailor the composition, particle size and morphology, and the crystallinity of the electrodeposited semiconductor toward specific applications. Similarly, much experience has accumulated on graphene electrochemistry,[53,54] which suggests that high quality graphene (or few-layer graphene), obtained by CVD, will be a more versatile electrode materials than their liquid phase exfoliated and partially reduced counterparts (rGO).

In this contribution, we aim to uncover the reasons behind the improved PEC performance of nanocarbon based photoelectrodes, compared to the bare semiconductor counterpart. To this end, various nanostructured carbon electrodes were prepared, including CNT networks, spray-coated graphene films (using LPE few-layer graphene platelets), and 3D graphene foams. Variable amounts of p-$Cu_2O$ was loaded on their surface via controlled electrochemical deposition, to explore a broad compositional and morphological space. By comparing and contrasting the PEC behavior of these hybrid photocathodes, we present a comprehensive analysis of the beneficial effects of various nanocarbon scaffolds, with primary focus on graphene. The main outcome of this study is that both the high surface area and the improved charge carrier separation and transport contribute to the enhanced PEC properties. After allowing for the effect of the different surface areas, it was possible to compare the nanocarbons with different morphology. Importantly, the 3D graphene architecture significantly outperformed its random/nonoriented counterparts. This trend was semiquantitatively supported by transient photocurrent measurements, where the magnitude of charge carrier recombination at the surface was estimated. The presented structure−property relationships can be exploited in the rational design of hybrid photoelectrodes *in general*, to obtain potentially attractive candidates for PEC energy conversion schemes, such as water splitting or $CO_2$ reduction.

## EXPERIMENTAL SECTION

**3D Graphene Foam Synthesis.** 3D graphene (3D-GR) foam was prepared via a CVD process using methane as the carbon source. The nickel foam (MTI Corporation, surface density: 350 g $m^{-2}$) was cleaned by successive sonication for 20 min in ethanol and water. A 1 cm × 3 cm piece of cleaned nickel foam was placed at the center of a fused quartz tube furnace (Lindberg Blue M, inner diameter 22 mm). The furnace tube was evacuated and then heated to 1000 °C with a 40 sccm $H_2$ gas flow under atmospheric pressure. After annealing for 20 min under these conditions, methane was introduced into the reactor. The temperature and gas flows were maintained in the furnace tube for 2 h. After the growth period, the Ar gas flow was stopped and the sample was cooled to room temperature under 40 sccm $H_2$ gas flow. Finally, the samples were immersed in 1 mol $dm^{-3}$ $FeCl_3$ overnight to dissolve the Ni foam and isolate the free-standing 3D graphene.[52]

**Electrode Preparation.** Premium-quality graphene powder (exfoliated graphene platelets from Elicarb) or home-grown arrays of CNTs[42] were dispersed in absolute ethanol by ultrasonic treatment. The formed dispersion (graphene: $c$ = 1 mg $mL^{-1}$, CNT: $c \approx 100$ $\mu$g $mL^{-1}$) was spray-coated on ultrasonically cleaned (5−5 min in acetone and ethanol) and preheated indium doped tin oxide-coated glass (ITO) electrodes, using an Alder AD320 type airbrush with a custom-made fully automated spray coater machine (operated with 1 bar compressed air). During the spray-coating process, the electrodes were masked to have an exposed surface area of 1 $cm^2$. To remove ethanol traces and to enhance adhesion of the graphene platelets or the CNTs, the electrodes were kept in an oven (180 °C) for 30 min. Graphene and CNT loading of the electrodes was controlled with the number of spray steps (GR1−6, 30−560 $\mu$g $cm^{-2}$, CNT: 35−690 $\mu$g $cm^{-2}$, see also Table S1), and quantified by quartz crystal microbalance (QCM) measurements using a Stanford Research System QCM-200 type instrument. The 3D graphene samples were fixed on a glass sheet by a small piece of a double-sided tape, and were contacted at the top by graphite adhesive to form the working electrode.

**$Cu_2O$ Electrodeposition.** All chemicals used were of analytical grade and were used as received. $CuSO_4 \times 5H_2O$ and $Na_2SO_4$ were purchased from Alfa Aesar, NaOH from VWR International, lactic acid


DOI: 10.1021/jacs.7b01820
J. Am. Chem. Soc. 2017, 139, 6682−6692

was from Sigma-Aldrich. Ultrapure water ($\rho$ = 18.2 MΩ cm, produced with a Millipore Direct Q3-UV instrument) was used for the preparation of all aqueous solutions. The nanocarbon electrodes were employed as the working electrode, while a Pt sheet and a Ag/AgCl/3 M NaCl were used as counter and reference electrodes, respectively. $Cu_2O$ was electrodeposited from an alkaline solution of lactate-stabilized copper sulfate, containing 0.4 mol $dm^{-3}$ cupric sulfate and 3 mol $dm^{-3}$ lactic acid in deionized water.[42] The pH was adjusted to 9 by the addition of concentrated sodium hydroxide solution. The electrodeposition was performed in a temperature-controlled classical three electrode electrochemical cell. The temperature of the solution was maintained at 60 °C, and the solution was constantly stirred by a magnetic stirrer during the electrodeposition. After recording linear sweep voltammetry data (Figure S2), multiple step potentiostatic electrodeposition protocols were employed (Figure 1).

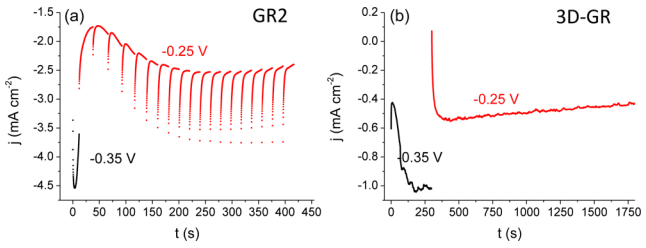


**Figure 1.** (a) Current response of a GR2/ITO electrode, while applying the multiple-potential step protocol. (b) Current−time curves, registered during the two-step potentiostatic electrodeposition of $Cu_2O$ on a 3D-GR electrode. Both syntheses were performed in 0.4 mol $dm^{-3}$ cupric sulfate and 3 mol $dm^{-3}$ lactate solution, at pH = 9 and $T$ = 60 °C.

All electrochemical measurements were performed on a Metrohm Autolab PGSTAT302 type potentiostat/galvanostat, equipped with an FRA32 type module for the impedance spectroscopic and the current transient measurements. To establish structure−property relationships, the thickness of the nanocarbon films (CNT: 35−690 $\mu$g $cm^{-2}$, graphene 30−560 $\mu$g $cm^{-2}$), as well as the amount of the electrodeposited $Cu_2O$ was systematically varied (50−2000 mC $cm^{-2}$). Cyclic voltammograms were recorded to estimate the actual surface area of the electrodes (see further discussion in the SI).

**Physical Characterization.** Raman spectroscopy was performed on a DXR Raman Microscope using a green laser ($\lambda$ = 532 nm), operating at 10 mW laser power. A FEI Tecnai $G^2$ 20 X-Twin type instrument, operating at an acceleration voltage of 200 kV, was used for transmission electron microscopy (TEM). Scanning electron microscopy (SEM) images were recorded on a Hitachi S-4700 field emission scanning electron microscope (coupled with a Röntec EDX detector), operating at an acceleration voltage of 10 kV. X-ray diffraction (XRD) patterns were recorded between $2\theta$ = 20−80° at 1° per minute scan rate on a Rigaku Miniflex II instrument, operating with a Cu $K_{\alpha,1}$ radiation source ($\lambda$ = 0.1541 nm). Diffuse reflectance UV−visible (DR UV−vis) spectra were recorded on an Avantes AVASpec-2048 type instrument, equipped with an AvaSphere-30 type integrating sphere. X-ray photoelectron spectra were recorded with a SPECS instrument equipped with a PHOIBOS 150 MCD 9 hemispherical analyzer. The analyzer was operated in the fixed analyzer transmission (FAT) mode with 20 eV pass energy. The Al K$\alpha$ radiation ($h\nu$ = 1486.6 eV) of a dual anode X-ray gun was used as the excitation source. The gun was operated at 210 W power (14 kV, 15 mA). The binding energy scale was corrected by fixing the main C 1s component to 285.0 eV, corresponding to adventitious carbon. For spectrum acquisition and evaluation both manufacturers (SpecsLab2) and commercial (CasaXPS, Origin) software packages were used. Electrochemical impedance spectra (EIS) of the hybrid films were recorded at open-circuit potential in the 10 Hz to 10 kHz frequency range, using a sinusoidal excitation signal (10 mV RMS amplitude). Modulus weighted fitting was performed using the Nova Software of the Autolab Instrument. For Mott−Schottky analysis, the full impedance spectra of the electrodes were recorded at different potentials ($E$ = 0.1−0.35 V vs Ag/AgCl/3 M NaCl).

**Photoelectrochemical Measurements.** Photovoltammograms were recorded in a sealed electrochemical cell made of quartz. To eliminate the effect of pH, photovoltammograms were recorded in $N_2$-saturated phosphate buffer (pH = 4.0, equal to the pH of the $CO_2$ saturated 0.1 mol $dm^{-3}$ $Na_2SO_4$) solutions as well. The solutions were saturated with $N_2$ or $CO_2$ by bubbling the gases through the cell for 30 min before and during the measurements (by forming a gas pillow above the solutions in the latter case). Linear sweep photovoltammograms were recorded under periodically interrupted light irradiation, using a Newport LCS-100 type solar simulator), operated at full output with a UV-cutoff filter (<400 nm), always placed at a fixed distance of 8 cm from the working electrode. Fast photocurrent transient measurements were performed using the same arrangement. During this measurement, data collection frequency was 20 kHz at five different potentials. Long-term $CO_2$ photoelectrolysis tests were performed in a two-compartment, sealed electrochemical cell (separated by a Nafion-117 membrane). The electrode potential was kept at a given value (−0.05 and +0.05 V vs Ag/AgCl/3 M NaCl), and the electrode was irradiated with the above-described periodically interrupted light source (at 0.033 Hz). Incident photon-to-electron conversion efficiency (IPCE) measurements were performed on a Newport Quantum Efficiency Measurement System (QEPVSI-B) in a single-compartment, three electrode quartz electrochemical cell. The wavelength range was 360−600 nm ($\Delta\lambda$ = 10 nm step size). The IPCE profiles were recorded at $E$ = 0.0 V, in $CO_2$ saturated 0.1 mol $dm^{-3}$ $Na_2SO_4$ solution.

Liquid and gas aliquots were taken regularly during photoelectrolysis. The $CO_2$ reduction products in the gas phase were analyzed with a Shimadzu GC-2010 Plus gas-chromatograph equipped with a barrier discharge ionization detector (BID). A HP-PLOT Molisieve column was used for the separation. Samples from the gas phase were taken at 5, 25, 50, and 70 min with a gastight syringe and injected into the GC with split injection. Heating procedure: 40 °C (6 min) to 30 °C/min −200 °C (4 min), injection temperature: 250 °C, linear velocity: 45.6 cm/s, split ratio: 40. The liquid-phase products were analyzed with a Shimadzu GC−MS QP 2010S gas chromatograph−mass spectrometer (column: ZB-FFAP) after removing the electrolyte ions with an Amberlite IRN-150 ion-exchange resin. Liquid samples were taken a few seconds after the gas samples. Heating procedure: 40 °C (3.5 min) to 50 °C/min −70 °C to 10 °C/min 170 °C to 50 °C/min −250 °C (5 min), injection temperature: 200 °C, linear velocity: 40 cm/s, split ratio: 10.

## RESULTS AND DISCUSSION

**Electrodeposition of $Cu_2O$/Graphene Composites.** Electrodeposition of the $Cu_2O$ nanoparticles on the nanocarbon substrates was realized by a multiple-step potentiostatic method (Figure 1). On the basis of linear sweep voltammetric data (Figure S2), a first nucleation step was conducted at $E$ = −0.35 V to initialize the formation of small seed particles, followed by one or more slow crystal growth steps at a less negative potential ($E$ = −0.25 V). For the spray-coated graphene samples, multiple growth steps were applied to introduce rest periods allowing for continuous supply of copper ions from the bulk solution. We emphasize that although the prenucleation step leads to some copper traces in the formed cuprous oxide, it was found to be essential to reach homogeneous coverage of the nanocarbon supports.

When this step was omitted, crystal formation occurred *exclusively* on the edges of graphene sheets (see the inset in Figure 4d). In agreement with our earlier results on $Cu_2O$ decorated carbon nanotubes,[26,42] we can conclude that homogeneous coverage of carbon nanostructures necessitates the application of a larger driving force (i.e., deposition potential), otherwise only the energetically preferred defect


DOI: 10.1021/jacs.7b01820
J. Am. Chem. Soc. 2017, 139, 6682−6692

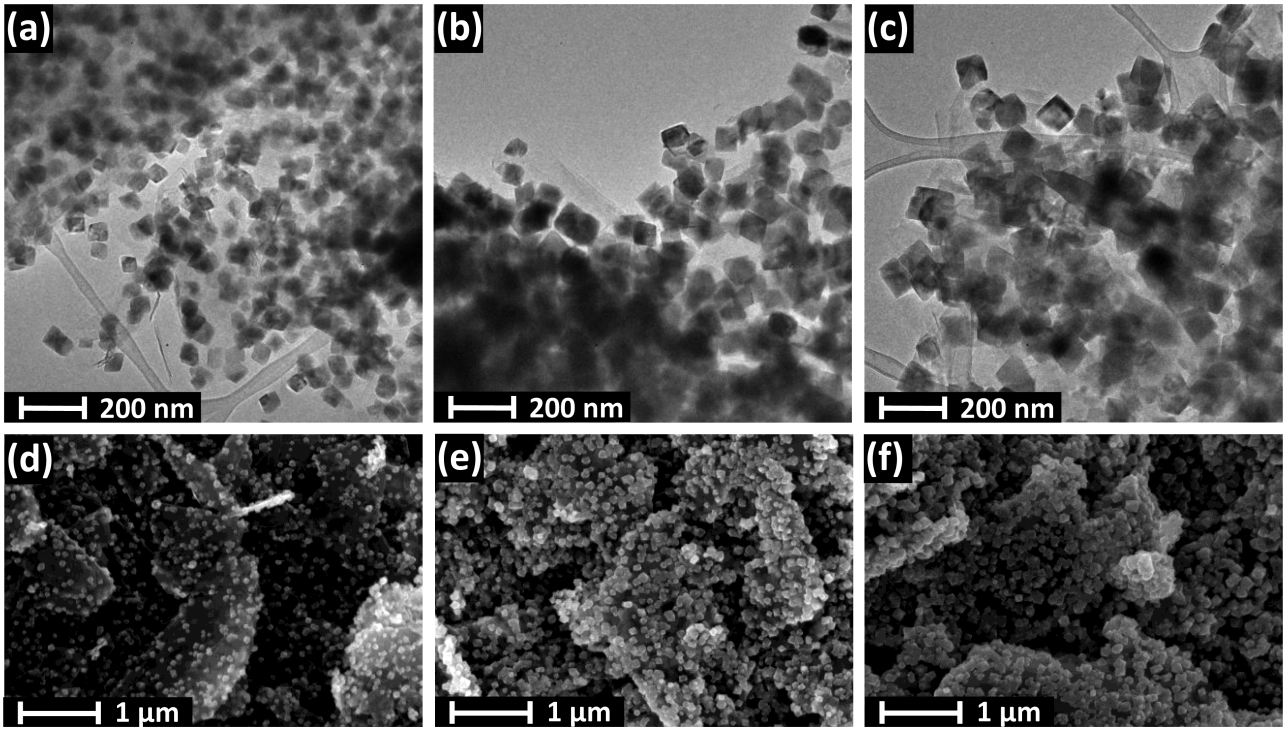


**Figure 2.** TEM images of $Cu_2O$/GR4 hybrids obtained with the deposition protocol shown in Figure 1a. The deposition charges were (a) 200 mC $cm^{-2}$, (b) 600 mC $cm^{-2}$, and (c) 1000 mC $cm^{-2}$. SEM images are also shown for the same samples (d–f).

places (e.g., edges, amorphous carbon traces, and grain boundaries) are covered by the electrodeposited $Cu_2O$.

Electron microscopy images were taken for the hybrid $Cu_2O$/GR samples with various compositions to probe their morphological attributes. TEM images confirmed that the $Cu_2O$ nanocrystallites are evenly dispersed on the graphene flakes (see Figure 2 and also Figure S3 for more images at both lower and higher magnifications). Additionally, it was also demonstrated that both the size and density of the nanoparticles can be effectively controlled by tuning the deposition protocol (i.e., the transferred charge). As seen in Figure 2 (from left to right), the growing deposition charge (from 200 mC $cm^{-2}$ to 1 C $cm^{-2}$) resulted in a gradual increase in both the surface coverage and the particle size. Specifically, the mean particle diameter shifted from 50 to 110 nm as deduced from the histograms in Figure 3. SEM images further confirmed the even dispersion of $Cu_2O$ nanoparticles on the graphene platelets (Figure 2d,e). SEM images were also taken for the bare $Cu_2O$ film on an ITO electrode (Figure S4). Most importantly, the crystallite sizes were much larger in this case, due to the smaller actual electrode surface area (note that the amount of the deposited $Cu_2O$ was identical).

For the 3D graphene-based hybrids, the graphene platelets were homogeneously and almost completely covered with octahedral $Cu_2O$ nanoparticles (see also Figure S5 for elemental mapping by EDX), having a size in the range of 100–150 nm (Figure 4). For this system, the initial nucleation step was indeed required to avoid specific deposition at the edge of the graphene platelets (compare with the inset in Figure 4d). Finally, we note that the original structure of the 3D graphene support was preserved in the nanocomposite; it did not suffer any major damage during the electrochemical deposition.

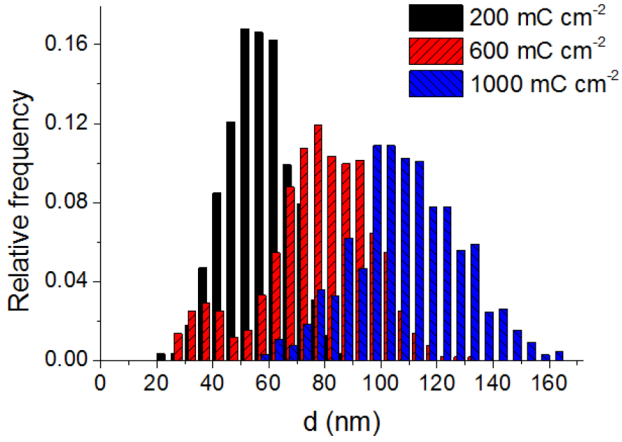


**Figure 3.** Particle size distribution for the same samples presented in Figure 2. The data were gathered from the TEM images, by measuring the size of 300 particles in each case.

Physical characterization was performed for all the prepared composite systems. The results were very similar for all the samples, confirming that there is no difference in the physicochemical properties of the deposited $Cu_2O$ in the different hybrid configurations. For the sake of brevity, we only present the results obtained for the $Cu_2O$/3D-GR composite, and emphasize any differences for the other hybrids. XRD patterns of the $Cu_2O$/graphene composites were recorded to identify the crystal structure and composition of the deposited oxide. The four most intense reflections of the $Cu_2O$ can be recognized (Figure 5a).[55] Although the presence of some copper traces cannot be completely excluded, the fact that reflections related to copper cannot be identified confirmed that this amount was negligible, if any. We note here that XPS data also confirmed that no Cu was formed during electro-



DOI: 10.1021/jacs.7b01820
J. Am. Chem. Soc. 2017, 139, 6682–6692

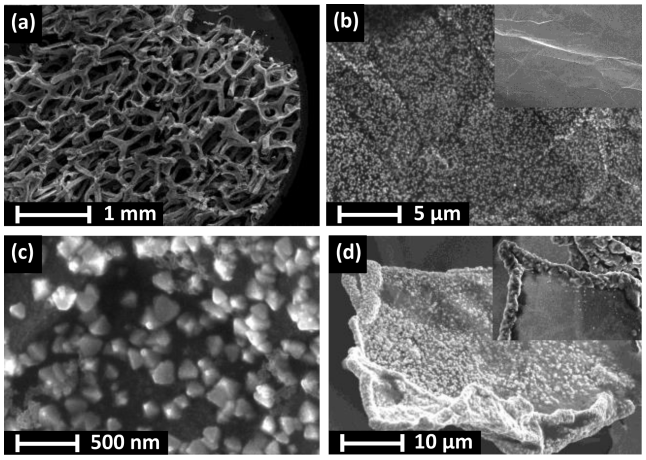


**Figure 4.** SEM images of a $Cu_2O$/3D-GR composite (deposited with 1 C $cm^{-2}$ charge density) at different magnifications. The inset on (b) shows the bare graphene surface while in (d) it shows the structure of the composite formed without the prenucleation step.

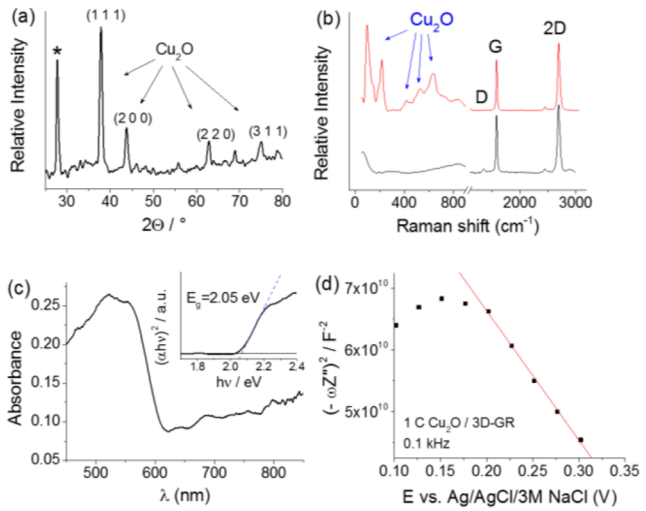


**Figure 5.** (a) XRD pattern, (b) Raman spectrum (also for the bare 3D-GR sample), (c) Diffuse-reflectance UV–vis spectrum (together with Tauc representation as inset), and (d) Mott–Schottky plot (recorded in 0.1 M NaAc solution), of a $Cu_2O$/3D-GR composite, deposited with 1 C $cm^{-2}$ charge density. The diffraction marked with asterisk in (a) corresponds to the graphene substrate.

deposition of $Cu_2O$ (see the lack of Cu (0) peak around 918.6 eV at the Auger spectrum, Figure S6B).

The appearance of the diffraction at $2\theta = 27.8°$ (marked with asterisk in Figure 5a) indicated that we have a multilayer graphene structure instead of a graphene monolayer, as the CVD-grown 3D graphene samples typically consist of both one- and few-layer domains.[52] This observation is typical for CVD-grown 3D graphene samples and contributes to the mechanical stability of the 3D electrode.[56]

The Raman spectrum of the composite showed all the characteristic Raman active vibration modes of $Cu_2O$ (Figure 5b). The appearance of the peaks at 145, 220, 416, 532, and 631 $cm^{-1}$ proves that $Cu_2O$ was formed during the deposition.[57,58] The lack of the characteristic vibration modes of CuO at 297 and 350 $cm^{-1}$ proved that the formed oxide is exclusively $Cu_2O$ and not CuO (confirming XRD results).[59] At 1582.5 $cm^{-1}$, the G-band of the graphene substrate, associated with the $E_{2g}$ vibration mode of the $sp^2$ framework,[60] can be discerned on the Raman spectrum.[61] The presence of a very small D-band at 1374 $cm^{-1}$ indicated that only trace amounts of defects were present in the nanocarbon template. Importantly, these defects were already present before synthesis of the composites, as seen from the spectrum of the bare 3D-GR sample. The intense 2D band centered at 2698 $cm^{-1}$ confirmed the few-layer character of the 3D-GR sample.

The optical bandgap of the $Cu_2O$/3D-GR composite was determined by diffuse reflectance UV–vis spectroscopy, and the spectrum was analyzed using a Tauc plot (see an example for the 3D-GR support in Figure 5c). The determined $E_g = 2.05$ eV was in good agreement with values reported for $Cu_2O$.[62] Similar data were collected for all $Cu_2O$/nanocarbon samples (not shown here). The most important conclusions were the following: (i) the absorption edge (related to $Cu_2O$, $E_g = 2.05$ eV, see also Figure 5C) of the samples did not alter with the varying graphene content and (ii) there was a massively increased noncharacteristic absorption related to graphene (especially in the vis-NIR region[30,63]).

Electrochemical impedance spectroscopic (EIS) measurements were carried out to determine the flatband potential of the composite (Figure 5d). By performing the Mott–Schottky analysis on the measured data, a flatband potential of $E = +0.51$ V (vs Ag/Ag/3 M NaCl) was obtained for the $Cu_2O$/3D-GR sample, a value slightly higher compared to data reported for electrodeposited $Cu_2O$ at neutral pH.[64,65] To compare the flatband potential (and thus the apparent Fermi level) of the various photoelectrodes, Table S2 summarizes the onset potential of the photovoltammetry profiles, the open circuit potentials with and without illumination, and the flatband potential obtained from the Mott–Schottky plots. The most important trend observed in these comparisons was the slight positive shift in the flatband potential (apparent Fermi level) in the case of the composite samples (compared to the bare $Cu_2O$). The magnitude of this shift increased with increasing nanocarbon loading, and had a maximum of 100 mV for the spray-coated carbons and 200 mV for the 3D-GR sample. These shifts indicate the intimate contact between the constituents, similar to trends in other studies in the literature on different semiconductor/nanocarbon assemblies.[29,30,32,63]

**Photoelectrochemical Properties.** To evaluate the PEC properties of the $Cu_2O$/graphene composites, the photoreduction of $CO_2$ was performed as a model reaction of practical significance (Figure 6a). The most important conclusions to be drawn from these initial measurements are the following: (i) The nanocomposite showed PEC activity toward $CO_2$ reduction, as confirmed by the enhanced photocurrents in the presence of $CO_2$ (note that the pH-effect was deconvoluted by performing control measurements in $N_2$ saturated solution, buffered to pH = 4.0, the pH of the $CO_2$ saturated solution); (ii) There was an increased photocurrent for the GR containing samples as compared to the bare oxide (Figure 6b); and (iii) The overall shape of the photovoltammograms was similar in the presence/absence of the carbon scaffold, except the development of a dark current in the case of the hybrids.

Additionally, both the onset potential of the $CO_2$ reduction and the maximum photocurrent were very similar to those determined earlier for $Cu_2O$/CNT composites,[42] but the shape of the linear sweep voltammetry (LSV) curve was somewhat different. In this case, the photocurrent did not decrease after a certain potential; it was stable in the presented potential


DOI: 10.1021/jacs.7b01820
J. Am. Chem. Soc. 2017, 139, 6682–6692

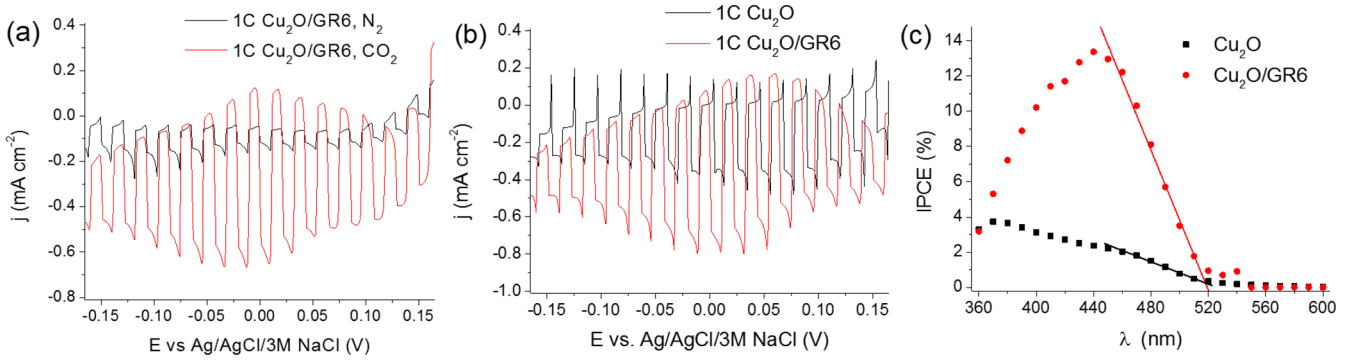


**Figure 6.** Linear sweep photovoltammograms recorded for (a) a $Cu_2O$/GR6 hybrid sample (1 C $cm^{-2}$ $Cu_2O$) in $CO_2$ or $N_2$ saturated 0.1 mol $dm^{-3}$ $Na_2SO_4$ (having the same pH = 4.0). (b) LSV curves for a $Cu_2O$/GR6 hybrid and a $Cu_2O$ film (1 C $cm^{-2}$ $Cu_2O$) in $CO_2$ saturated 0.1 mol $dm^{-3}$ $Na_2SO_4$ solution. The sweep rate was kept at 2 mV $s^{-1}$, while the light-chopping frequency was 0.2 Hz. A solar simulator was used employing a UV cutoff filter (<400 nm). (c) Photoaction spectra for the two electrodes presented in (b), recorded at $E$ = 0.0 V (vs Ag/AgCl/3 M NaCl) in $CO_2$ saturated 0.1 mol $dm^{-3}$ $Na_2SO_4$ solution.

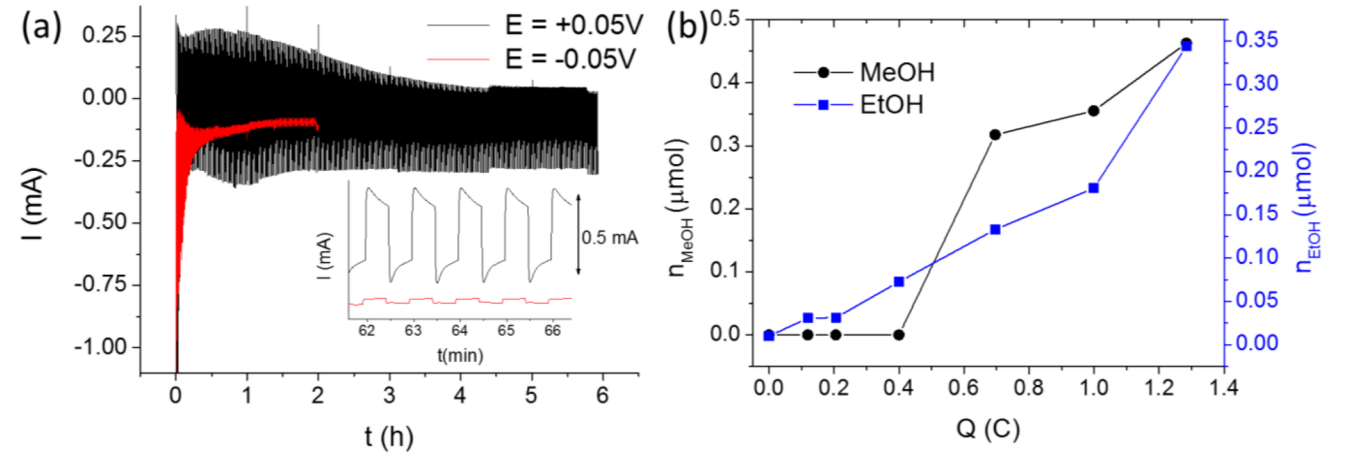


**Figure 7.** (a) Long-term chronoamperometry data of two $Cu_2O$/GR6 electrodes with an identical $Cu_2O$ content (1 C), registered at $E$ = +0.05 V and $E$ = −0.05 V potential (vs Ag/AgCl/3 M NaCl), in $CO_2$ saturated 0.1 M $Na_2SO_4$ solution. A solar simulator was used employing a UV cutoff filter (<400 nm). (b) Formation of alcohols during the photoelectrolysis presented in (a).

regime. Photoaction spectra (incident photon to current efficiency (IPCE) vs wavelength) were recorded, and a massive increase in the IPCE values was observed on the photoaction spectrum (Figure 6c). The identical wavelength threshold value confirmed that the enhanced photocurrents were not related to some new absorption or bandgap shift, but indeed to the better charge carrier extraction in the hybrid (note that the amount of $Cu_2O$ was the same).

Long-term photoelectrolysis was performed at different potentials to assess the stability of the $Cu_2O$/GR electrode. As shown in Figure 7a, even a 100 mV shift in the external bias potential can cause a massive alteration in the overall shape. Specifically, at $E$ = −0.05 V, the rapid cessation of the photocurrents was seen, as a result of photocorrosion (i.e., formation of metallic Cu).[12] On the other hand, at $E$ = +0.05 V, stable photoactivity was reached after an initial decrease. This enhanced PEC behavior is attributed to the dark reoxidation of metallic copper moieties, formed via photocorrosion.[12] This hypothesis is supported by the initially observed dark anodic currents at this potential. Notably, a steady-state was reached after 2.5 h, with stable photocurrents and minor dark currents.

To verify that the increased photocurrents in the presence of $CO_2$ (see Figure 6a) were related to its conversion to useful products, aliquots were taken periodically both from the liquid and gas phases. Importantly, in the gas phase only minor traces of $H_2$ were detected and no CO formation was confirmed. As for the liquid phase, methanol, ethanol and minor amounts of formic acid were detected; similarly to earlier studies on $Cu_2O$-containing photoelectrodes.[42,66] Interestingly, while the ethanol concentration increased continuously, the methanol formation only started after the steady-state PEC behavior was reached (Figure 7b). Quantitatively, the two alcohols accounted for a Faradaic efficiency of 50−60% (with a 2:3 FE ratio for methanol/ethanol) while the rest of the charge was related to $H_2$ and formate production, and the photoreduction of $Cu_2O$ to Cu as detailed above. Comparative studies were performed with a bare $Cu_2O$ electrode, deposited with identical charge density (Figure S7). The formation of methanol and ethanol was witnessed, although with a different ratio (see additional discussion in the SI).

Degradation of the $Cu_2O$/3D-GR electrode structure during long-term photoelectrolysis is a relevant concern. We found that major degradation of the 3D structure only occurred when the photoelectrolysis was performed at more negative potentials, where water splitting (and thus $H_2$ bubble formation) also occurred. SEM images were taken for samples after photoelectrolysis, and are shown in Figure S9.

**Factors Behind the Improved PEC Properties.** To explore a broad range of the composition and morphology, the effect of the GR thickness and the deposited $Cu_2O$ amount


DOI: 10.1021/jacs.7b01820
J. Am. Chem. Soc. 2017, 139, 6682−6692

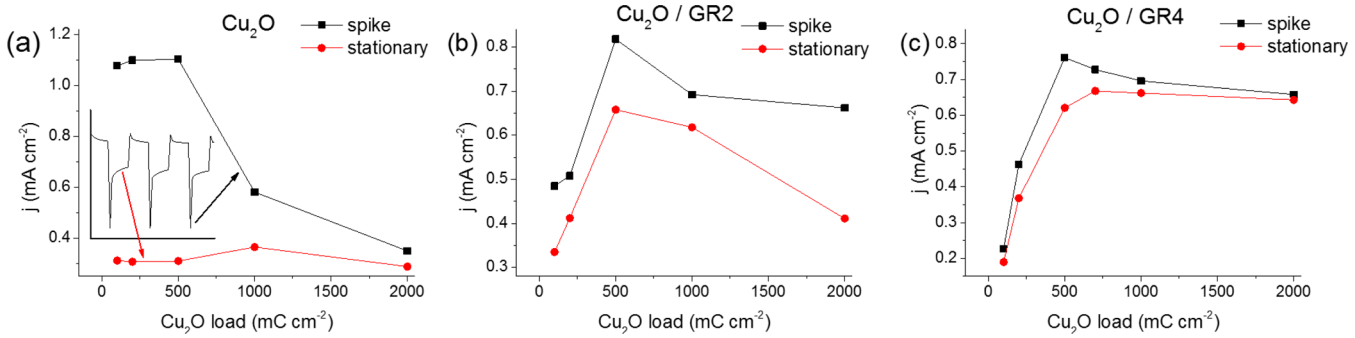


**Figure 8.** Comparison of the transient and stationary photocurrents at $E$ = +0.05 V, for five different $Cu_2O$ loadings (100−2000 mC $cm^{-2}$), on (a) a bare ITO and (b,c) two different GR/ITO supports. The inset in (a) shows how the data points were determined. The lines among the data points serve only to guide the eye.

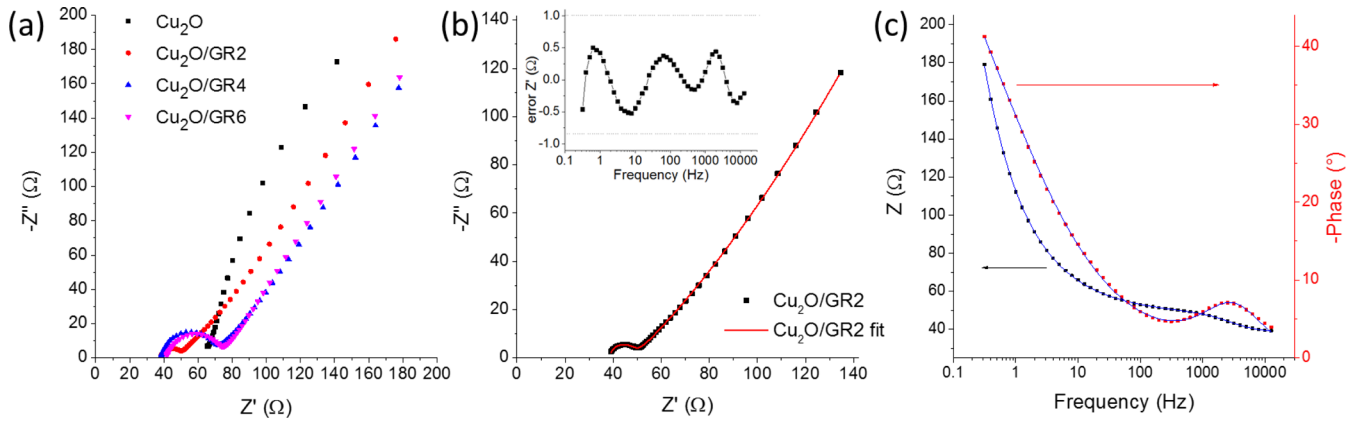


**Figure 9.** (a) Nyquist plots recorded for pristine $Cu_2O$ and three different $Cu_2O$/GR composites deposited with 1 C $cm^{-2}$ charge density, in 0.1 M sodium acetate solution at open circuit potential, in the 0.1 Hz to 10 kHz frequency range. (b) Measured (points) and simulated (solid line) Nyquist and (c) Bode-plots of a $Cu_2O$/GR electrode. The inset in (b) shows the error associated with the Bode plot fit (i.e., difference between the measured and calculated value).

were both varied systematically. Figure 8 compares the measured photocurrents (both the initial current spike and the stationary plateau; as shown in the inset of Figure 8a) for the bare $Cu_2O$ (on an ITO electrode) and composites (GR supports of three different thicknesses and five different $Cu_2O$ loadings for each support). As for the bare $Cu_2O$, there was a huge difference between the initial and the stationary photocurrent values. This observation suggests the insufficient charge carrier extraction in the case of the bare oxide (see below for detailed discussion of this point). In addition, the stationary photocurrents seemed to be independent of the $Cu_2O$ loading (film thickness), at least in the studied regime. This constant current suggests that the reacting photoelectrons come from a distinct region of the $Cu_2O$ film, independently from the thickness. The overall pattern was totally different for the $Cu_2O$/graphene composites (Figure 8b−c): (i) The transient and the stationary values were much closer to each other, confirming our assumption that the highly conductive graphene support facilitates effective charge separation and charge carrier extraction; (ii) The maximum photocurrent gradually shifts to higher $Cu_2O$ loadings with increasing graphene thickness. Similar experiments were carried out with the 3D graphene samples and the composition dependent PEC behavior was also confirmed (Figure S8). These trends suggest that there is an optimal composition (i.e., $Cu_2O$/graphene ratio) in the hybrid configuration.

While the effect of GR thickness can be studied by comparing samples with identical $Cu_2O$ content, their optical behavior might be different. In fact, this increased light absorption with higher GR thicknesses explains the decrease in the photocurrents at high GR thicknesses, where light absorption of $Cu_2O$ is hindered by the presence of GR. This trend is also reflected in Figure 10 below.

The question, however, still holds: what are the reasons behind the improvement in the PEC properties? EIS measurements were performed to scrutinize the electronic properties of the synthesized photoelectrodes. From qualitative analysis of the Nyquist plots depicted in Figure 9a, one can see the large decrease of semicircle size for the graphene-containing composites. Additionally, there is a higher series resistance for the $Cu_2O$/ITO sample compared to its graphene-containing counterparts (most likely rooted in the resistance of the $Cu_2O$/ITO interface). To quantify these trends an equivalent circuit (see the circuit and its description in the SI, Figure S10) was employed to fit the measured data (Figures 9b and c). The most important conclusions are the following: (i) There was a huge decrease (from 500 Ω to 10 Ω) in the charge transfer resistance ($R_{ct}$) when $Cu_2O$ was electrodeposited on the GR support instead of the bare ITO; (ii) When the GR thickness was increased the $R_{ct}$ value also increased to 30 Ω, and then remained constant at higher GR thicknesses; (iii) The very high surface area of the hybrid electrodes was reflected in the high double-layer capacitance values ($C_1$, 10−30 mF $cm^{-2}$). Overall,


DOI: 10.1021/jacs.7b01820
J. Am. Chem. Soc. 2017, 139, 6682−6692

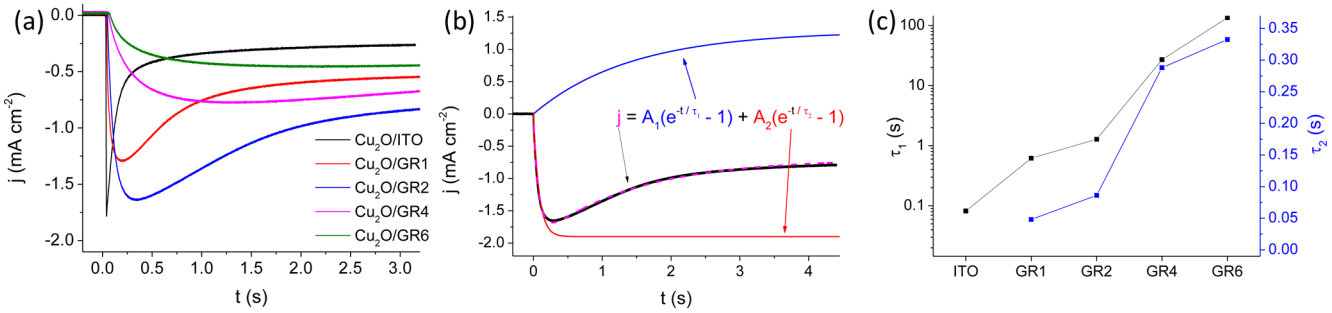


**Figure 10.** (a) Photocurrent transients of a pristine $Cu_2O$ film and four different $Cu_2O$/GR composites deposited with 0.5 C $cm^{-2}$ charge density, in $CO_2$ saturated 0.1 M $Na_2SO_4$ solution at $E$ = 0.05 V potential. A solar simulator was used employing a UV cutoff filter (<400 nm). (b) Dual exponential fit of a transient photocurrent response of the $Cu_2O$/GR2 sample. (c) Time constant values obtained for the samples shown in (a). The lines among the data points serve only to guide visualization.

these results confirm that the improved electrical conductivity, facilitating better charge carrier transport, is an important contributor to the superior PEC properties of the hybrid electrodes.

To get a better understanding on the charge carrier recombination process, transient photocurrent measurements were performed.[67−69] In these measurements the photocurrent was followed after the light was switched on (chopped illumination). The first important observation in all experiments was the slow relaxation of the cathodic photocurrents (on the order of seconds, see Figures 10 and 11). Similarly to

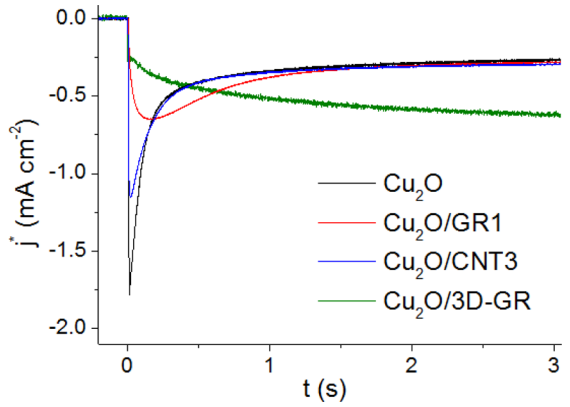


**Figure 11.** Photocurrent transient analysis of a pristine $Cu_2O$ film and three different $Cu_2O$/nanocarbon composites deposited with 0.5 C $cm^{-2}$ charge density. The measurements were performed in $CO_2$ saturated 0.1 M $Na_2SO_4$ solution at $E$ = 0.05 V potential. A solar simulator was used employing a UV cutoff filter (<400 nm). Photocurrent normalization was performed using the relative surface area data in Table S1.

previous water oxidation studies,[68,69] this slow charge transfer can be attributed to the kinetically hindered, multielectron nature of $CO_2$ reduction (i.e., it involves 6 $e^-$ and 6 $H^+$ to form methanol). The competition between electron transfer to $CO_2$ at electrode/electrolyte interface and electron−hole recombination within the space charge layer and at the surface means that only a portion of the photogenerated electrons can react with $CO_2$. Consequently, the achieved solar to chemical conversion efficiencies are much smaller than what could be expected from the optoelectronic properties of $Cu_2O$. Extensive recombination is particularly problematic close to the Fermi level, and while higher external bias potentials can help to suppress it, there is a trade off because of the needed additional energy input. Also note that the stability of the photoelectrode was much lower at higher bias potentials, see also Figure 7.

Transient photocurrent curves recorded for the different samples are compared and contrasted in Figure 10a. While for the bare $Cu_2O$ there was a sharp transient, this feature gradually disappeared in the series of $Cu_2O$/GR samples with progressively higher GR content. As for $Cu_2O$, the photocurrent developed instantaneously after the light was turned on, followed by an exponential decay to a steady-state cathodic value. These cathodic photocurrent transients can be attributed to accumulation of the photogenerated electrons in the $Cu_2O$ space charge layer and recombination of bulk holes with these electrons.[67−69] At longer time scales, a steady-state photocurrent was reached, the magnitude of which was dictated by the relative rates of recombination and charge transfer to redox species.[67]

As for the graphene containing samples, the pattern was more complex. First, the initial spike got gradually smaller and finally disappeared as the graphene thickness increased. Meanwhile, an opposite (i.e., increasing) pattern developed, dictated by charge carrier transport through the relatively thick $Cu_2O$/GR electrode architecture (note that no such behavior was observed for thin nanocarbon supports or bare $Cu_2O$, see also Figures 11 and S11). The relative contribution of these processes is clearly correlated with the graphene content (note that the $Cu_2O$ amount was identical in all cases). The ratio of the steady-state and the peak photocurrent increased with the graphene thickness, because of the increasing magnitude of $Cu_2O$/GR junction area (see also Figure 8). This suppressed recombination, however, did not result in constantly growing steady-state currents, mostly because of changing optoelectronic properties in the series of samples (i.e., light absorption of graphene (see above), increased resistance (see Figure 9)).

To facilitate quantitative comparison, the transient photocurrent curves were fitted and time constants were determined for all systems with different composition and morphology. The transient photocurrent curves could be well-fit to a sum of two exponential functions, one related to surface recombination (characterized by $\tau_1$) and another one dictated by hole-transport through the electrode assembly (characterized by $\tau_2$)[70] (see the fitted equation and an example of the fitting in Figure 10b). While $A_2$ gives the absolute value of the maximum achievable photocurrent (i.e., in the absence of recombination), $A_1$ shows the maximal contribution of the recombination process to the decrease in the photocurrent. As seen in Figure 10c, both time constants increased with the growing GR thickness, although at vastly different extents (note the


DOI: 10.1021/jacs.7b01820
J. Am. Chem. Soc. 2017, 139, 6682−6692

logarithmic scale for $\tau_1$). The time constant related to recombination increased rapidly with the higher graphene thicknesses. Note that the $Cu_2O$ amount was fixed, therefore this trend is related to the gradually thinner $Cu_2O$ coverage on the graphene platelets.

Upon light irradiation the photogenerated electrons (minority carriers) are driven toward the electrode/electrolyte interface by band bending, while the holes are rapidly siphoned off by the graphene phase (note that this process occurs on the nanosecond time scale).[71] As a net result, the time constant related to recombination increased by three orders of magnitude for the composite sample with the highest graphene content, compared to the bare $Cu_2O$ film. On the other hand, $\tau_2$ changed almost proportionally with the GR loading (thickness), which is not too surprising considering that this time constant is related to the transport of holes to the current collector (ITO). We also note here that there are several other processes which contribute to the charge carrier dynamics of the presented photoelectrodes. However, exciton generation, charge carrier separation in $Cu_2O$, and charge transfer from $Cu_2O$ to GR occur on a much shorter (fs−ns) time scale, so that their effect cannot be important here.[30,72] Pump−probe transient absorption laser spectroscopic studies are planned in the future to study these processes in operando. From these results taken as a whole, we may conclude that both the enhanced specific surface area and improved charge carrier transport result in suppressed recombination, so that a higher fraction of the photogenerated electrons can react with $CO_2$.

**Comparison of Graphene, 3D Graphene, and CNT as Photoelectrode Support.** Finally, to further elucidate the role of the nanocarbon scaffold and possible morphological aspects, the PEC behavior of different nanocarbon containing hybrid samples were compared. To deconvolute the effect of the different surface areas, samples with similar charge capacitance are compared in Figure 11, and the slight differences in the surface area were taken into account by normalizing the photocurrent values (see also Figure S1 and Table S1). The $Cu_2O$ content was identical in all cases (0.5 C $cm^{-2}$, with respect to the geometrical surface area). What is immediately striking is that steady-state currents on the three curves ($Cu_2O$, $Cu_2O$/CNT3, and $Cu_2O$/GR1) almost overlap after normalization, although they have significantly different time constants (slower recombination for CNT and especially the GR-containing composite, compared to the bare $Cu_2O$). These trends suggest that in these instances the improved PEC activity shown above (e.g., Figures 6 and 8) is predominantly rooted in the increased surface area (and the resultant high $Cu_2O$/carbon junction area), provided by the highly conductive nanocarbon scaffold. After factoring out this effect, very similar behavior is seen, at least in terms of the steady-state photocurrents (see also Figure S12a).

On the other hand, much higher normalized steady-state photocurrent flow could be seen for the 3D-GR support, most likely because of the superior charge transport properties rooted in the lack of particle−particle interfaces (also consider that the size of graphene platelets is much higher in this case, compared to the spray-coated samples, see Figure 4 and Figure S3). Note that while this support had relatively small surface area, at the same time, it has a higher thickness. This manifested in the large time constant for the photocurrent development ($\tau_2$).

Finally, we recognize that the light penetration depth was limited in this macroscopic architecture. Consequently, design of other 3D architectures, where benefits of the presented 3D graphene structure could be maintained while simultaneously ensuring sufficient light harvesting, would be highly desirable; such studies are in progress in our laboratories.

## CONCLUSIONS

A broad compositional and morphological space was explored to assemble hybrid photoelectrodes based on a highly conductive nanocarbon support (graphene) and a p-type inorganic semiconductor ($Cu_2O$). A multiple potential-step electrodeposition protocol was employed to control the amount and size (thus the overall coverage) of the $Cu_2O$ nanocrystallites on the graphene surface. The PEC activity of the composites was proved in $CO_2$ reduction (to form alcohol products), as a model multielectron transfer reaction of practical significance. It was found that the graphene-containing photoelectrodes outperformed the pure $Cu_2O$, both in terms of the achieved current densities and stability. Composition-dependent PEC studies revealed that there was an optimal loading for both components. Transient photocurrent measurements revealed that the main contribution of the graphene substrate in such structures was the facilitation of effective charge separation and transport, leading to better harvesting of the generated photoelectrons. An added bonus is enhanced stability and durability of the semiconductor components.

A phenomenological model was developed involving: (i) electron transfer from $Cu_2O$ to $CO_2$, (ii) recombination of the photoelectrons with holes in the space charge layer, (iii) hole transfer from $Cu_2O$ to graphene, and (iv) hole transport through the electrode architecture to the current collector. By fitting the transient photocurrent curve, semiquantitative assessment could be made, for the first time, for the graphene contribution to the enhanced PEC activity of the hybrid photoelectrodes. The presented approach also afforded study of the effect of the nanocarbon morphology: after deconvoluting the effect of the increased surface area, we demonstrated that an interconnected 3D graphene structure (as a new promising member of the self-standing, highly conductive carbon derivative family) has further benefits compared to its nonorganized counterparts (spray-coated graphene and CNT films), because of the lack of carbon−carbon boundaries in the structure. Importantly, the presented design elements for the new family of photoelectrode materials in this study can be utilized for solar fuels generation *in general*, by assembling hybrid architectures with complementary function and optimized nanomorphology.

## ASSOCIATED CONTENT

### Supporting Information

The Supporting Information is available free of charge on the ACS Publications website at DOI: 10.1021/jacs.7b01820.

Additional synthetic details, morphological studies, EIS data, and photoelectrochemical analysis (PDF)

## AUTHOR INFORMATION


### Corresponding Author

*janaky@chem.u-szeged.hu

### ORCID

Robert A. W. Dryfe: 0000-0002-9335-4451
Krishnan Rajeshwar: 0000-0003-4917-7790
Csaba Janáky: 0000-0001-5965-5173




DOI: 10.1021/jacs.7b01820
J. Am. Chem. Soc. 2017, 139, 6682−6692

### Notes

The authors declare no competing financial interest.

## ■ ACKNOWLEDGMENTS

This project has received funding from the European Research Council (ERC) under the European Union's Horizon 2020 research and innovation programme (grant agreement No 716539). The authors also thank Rendernet Ltd. for assistance in preparing the artwork in the TOC. This research was partially supported by the "Széchenyi 2020" program in the framework of GINOP-2.3.2-15-2016-00013 "Intelligent materials based on functional surfaces—from syntheses to applications" project. Authors from the University of Manchester were supported by EPSRC grants (EP/K007033/1 and EP/K016954/1). The authors thank Dr. Tamás Pajkossy (Research Center for Natural Sciences of the Hungarian Academy of Sciences) for the valuable discussions on the EIS results, Dorottya Hursán for the support with the GC−MS analysis, and Dr. Albert Oszkó (University of Szeged) for recording the XPS spectra during the peer review cycle. Finally, the authors thank the three anonymous reviewers for their constructive and insightful criticisms of an earlier manuscript version.

## ■ REFERENCES

(1) Lewis, N. S.; Nocera, D. G. *Proc. Natl. Acad. Sci. U. S. A.* **2006**, *103*, 15729−15735.
(2) Wang, H.; Dai, H. *Chem. Soc. Rev.* **2013**, *42*, 3088−3113.
(3) Joshi, U. A.; Palasyuk, A.; Arney, D.; Maggard, P. A. *J. Phys. Chem. Lett.* **2010**, *1*, 2719−2726.
(4) Sivula, K. *J. Phys. Chem. Lett.* **2015**, *6*, 1624−1633.
(5) Rajeshwar, K. *J. Phys. Chem. Lett.* **2011**, *2*, 1301−1309.
(6) Fujishima, A.; Honda, K. *Nature* **1972**, *238*, 37−38.
(7) Cowan, A. J.; Durrant, J. R. *Chem. Soc. Rev.* **2013**, *42*, 2281−2293.
(8) Boston, D.; Huang, K.-L.; de Tacconi, N.; Myung, N.; MacDonell, F.; Rajeshwar, K. Chapter 11. Electro- and Photocatalytic Reduction of $CO_2$: The Homogeneous and Heterogeneous Worlds Collide? In *Photoelectrochemical Water Splitting: Materials, Processes and Architectures*; Lewerenz, H.-J., Peter, L., Eds.; The Royal Society of Chemistry, 2013.
(9) Kumar, B.; Llorente, M.; Froehlich, J.; Dang, T.; Sathrum, A.; Kubiak, C. P. *Annu. Rev. Phys. Chem.* **2012**, *63*, 541−569.
(10) Taniguchi, I.; Aurian-Blajeni, B.; Bockris, J. *Electrochim. Acta* **1984**, *29*, 923−932.
(11) Ghadimkhani, G.; de Tacconi, N. R.; Chanmanee, W.; Janaky, C.; Rajeshwar, K. *Chem. Commun.* **2013**, *49*, 1297−1299.
(12) Janaky, C.; Hursán, D.; Endrodi, B.; Chanmanee, W.; Roy, D.; Liu, D.; Tacconi, N. R. De; Dennis, B. H.; Rajeshwar, K. *ACS Energy Lett.* **2016**, *1*, 332−338.
(13) Read, C. G.; Park, Y.; Choi, K. S. *J. Phys. Chem. Lett.* **2013**, *3*, 1872−1876.
(14) Gu, J.; Wuttig, A.; Krizan, J. W.; Hu, Y.; Detweiler, Z. M.; Cava, R. J.; Bocarsly, A. B. *J. Phys. Chem. C* **2013**, *117*, 12415−12422.
(15) Prévot, M. S.; Guijarro, N.; Sivula, K. *ChemSusChem* **2015**, *8*, 1359−1367.
(16) Sharma, G.; Zhao, Z.; Sarker, P.; Nail, B. A.; Wang, J.; Huda, M. N.; Osterloh, F. E. *J. Mater. Chem. A* **2016**, *4*, 2936−2942.
(17) Kormányos, A.; Thomas, A.; Huda, M. N.; Sarker, P.; Liu, J. P.; Poudyal, N.; Janáky, C.; Rajeshwar, K. *J. Phys. Chem. C* **2016**, *120*, 16024−16034.
(18) Jang, J.-W.; Cho, S.; Magesh, G.; Jang, Y. J.; Kim, J. Y.; Kim, W. Y.; Seo, J. K.; Kim, S.; Lee, K.-H.; Lee, J. S. *Angew. Chem., Int. Ed.* **2014**, *53*, 5852−5857.
(19) Kang, U.; Choi, S. K.; Ham, D. J.; Ji, S. M.; Choi, W.; Han, D. S.; Abdel-Wahab, A.; Park, H. *Energy Environ. Sci.* **2015**, *8*, 2638−2643.
(20) Halmann, M. *Nature* **1978**, *275*, 115−116.
(21) Bockris, J.; Wass, J. C. *Mater. Chem. Phys.* **1989**, *22*, 249−280.
(22) Barton, E.; Rampulla, D. M.; Bocarsly, A. B. *J. Am. Chem. Soc.* **2008**, *130*, 6342−6344.
(23) Appel, A. M.; Bercaw, J. E.; Bocarsly, A. B.; Dobbek, H.; Dubois, D. L.; Dupuis, M.; Ferry, J. G.; Fujita, E.; Hille, R.; Kenis, P. J. A; Kerfeld, C. A.; Morris, R. H.; Peden, C. H. F.; Portis, A. R.; Ragsdale, S. W.; Rauchfuss, T. B.; Reek, J. N. H.; Seefeldt, L. C.; Thauer, R. K.; Waldrop, G. L. *Chem. Rev.* **2013**, *113*, 6621−6658.
(24) Sivula, K. *J. Phys. Chem. Lett.* **2015**, *6*, 975−976.
(25) Janáky, C.; Rajeshwar, K. *Prog. Polym. Sci.* **2015**, *43*, 96−135.
(26) Janáky, C.; Kecsenovity, E.; Rajeshwar, K. *ChemElectroChem* **2016**, *3*, 181−192.
(27) Thangavel, S.; Krishnamoorthy, K.; Krishnaswamy, V.; Raju, N.; Kim, S. J.; Venugopal, G. *J. Phys. Chem. C* **2015**, *119*, 22057−22065.
(28) Thangavel, S.; Krishnamoorthy, K.; Kim, S.; Venugopal, G. *J. Alloys Compd.* **2016**, *683*, 456−462.
(29) Kongkanand, A.; Martínez Domínguez, R.; Kamat, P. V. *Nano Lett.* **2007**, *7*, 676−680.
(30) Meng, F.; Li, J.; Cushing, S. K.; Bright, J.; Zhi, M.; Rowley, J. D.; Hong, Z.; Manivannan, A.; Bristow, A. D.; Wu, N. *ACS Catal.* **2013**, *3* (4), 746−751.
(31) Meng, F.; Cushing, S. K.; Li, J.; Hao, S.; Wu, N. *ACS Catal.* **2015**, *5*, 1949−1955.
(32) Xiang, Q.; Yu, J.; Jaroniec, M. *Chem. Soc. Rev.* **2012**, *41*, 782−796.
(33) Yang, M.-Q.; Zhang, N.; Pagliaro, M.; Xu, Y.-J. *Chem. Soc. Rev.* **2014**, *43*, 8240−8254.
(34) Xiang, Q.; Cheng, B.; Yu, J. *Angew. Chem., Int. Ed.* **2015**, *54*, 11350−11366.
(35) Lightcap, I. V.; Kamat, P. V. *Acc. Chem. Res.* **2013**, *46*, 2235−2243.
(36) Yokomizo, Y.; Krishnamurthy, S.; Kamat, P. V. *Catal. Today* **2013**, *199*, 36−41.
(37) Pathak, P.; Gupta, S.; Grosulak, K.; Imahori, H.; Subramanian, V. *J. Phys. Chem. C* **2015**, *119*, 7543−7553.
(38) Yin, S.; Men, X.; Sun, H.; She, P.; Zhang, W.; Wu, C.; Qin, W.; Chen, X. *J. Mater. Chem. A* **2015**, *3*, 12016−12022.
(39) An, X.; Li, K.; Tang, J. *ChemSusChem* **2014**, *7*, 1086−1093.
(40) Liang, Y. T.; Vijayan, B. K.; Gray, K. A.; Hersam, M. C. *Nano Lett.* **2011**, *11*, 2865−2870.
(41) Ng, Y. H.; Iwase, A.; Kudo, A.; Amal, R. *J. Phys. Chem. Lett.* **2010**, *1*, 2607−2612.
(42) Kecsenovity, E.; Endrődi, B.; Pápa, Z.; Hernádi, K.; Rajeshwar, K.; Janáky, C. *J. Mater. Chem. A* **2016**, *4*, 3139−3147.
(43) Young Kim, J.; Jang, J.-W.; Hyun Youn, D.; Yul Kim, J.; Sun Kim, E.; Sung Lee, J. *RSC Adv.* **2012**, *2*, 9415.
(44) Zhang, Z.; Dua, R.; Zhang, L.; Zhu, H.; Zhang, H.; Wang, P. *ACS Nano* **2013**, *7*, 1709−1717.
(45) Yu, L.; Li, G.; Zhang, X.; Ba, X.; Shi, G.; Li, Y.; Wong, P. K.; Yu, J. C.; Yu, Y. *ACS Catal.* **2016**, *6*, 6444−6454.
(46) Hou, J.; Cheng, H.; Takeda, O.; Zhu, H. *Angew. Chem., Int. Ed.* **2015**, *54*, 8480−8484.
(47) Yang, M.-Q.; Xu, Y.-J. *Nanoscale Horiz.* **2016**, *1*, 185−200.
(48) Low, J.; Yu, J.; Ho, W. *J. Phys. Chem. Lett.* **2015**, *6*, 4244−4251.
(49) Low, J.; Cheng, B.; Yu, J.; Jaroniec, M. *Energy Storage Mater.* **2016**, *3*, 24−35.
(50) Dong, X.; Cao, Y.; Wang, J.; Chan-Park, M. B.; Wang, L.; Huang, W.; Chen, P. *RSC Adv.* **2012**, *2*, 4364−4369.
(51) Zhan, B. B.; Liu, C. B.; Chen, H. P.; Shi, H. X.; Wang, L. H.; Chen, P.; Huang, W.; Dong, X. C. *Nanoscale* **2014**, *6*, 7424−7429.
(52) Zou, Y.; Kinloch, I. A.; Dryfe, R. A. W. *ACS Appl. Mater. Interfaces* **2015**, *7*, 22831−22838.
(53) Ambrosi, A.; Chua, C. K.; Bonanni, A.; Pumera, M. *Chem. Rev.* **2014**, *114*, 7150−7188.
(54) Valota, A. T.; Toth, P. S.; Kim, Y.-J.; Hong, B. H.; Kinloch, I. A.; Novoselov, K. S.; Hill, E. W.; Dryfe, R. A. W. *Electrochim. Acta* **2013**, *110*, 9−15.
(55) Zhang, H.; Zhu, Q.; Zhang, Y.; Wang, Y.; Zhao, L.; Yu, B. *Adv. Funct. Mater.* **2007**, *17*, 2766−2771.


DOI: 10.1021/jacs.7b01820
*J. Am. Chem. Soc.* 2017, 139, 6682−6692

(56) Cao, X.; Yin, Z.; Zhang, H. *Energy Environ. Sci.* **2014**, *7*, 1850−1865.
(57) Huang, M.; Wang, T.; Chang, W.; Lin, J.; Wu, C.; Chen, I.-C.; Peng, K.; Lee, S. *Appl. Surf. Sci.* **2014**, *301*, 369−377.
(58) Mohemmed Shanid, N. A.; Abdul Khadar, M.; Sathe, V. G. *J. Raman Spectrosc.* **2011**, *42*, 1769−1773.
(59) Dar, M. A.; Kim, Y. S.; Kim, W. B.; Sohn, J. M.; Shin, H. S. *Appl. Surf. Sci.* **2008**, *254*, 7477−7481.
(60) Ferrari, A. C.; Meyer, J. C.; Scardaci, V.; Casiraghi, C.; Lazzeri, M.; Mauri, F.; Piscanec, S.; Jiang, D.; Novoselov, K. S.; Roth, S.; Geim, A. K. *Phys. Rev. Lett.* **2006**, *97*, 187401−187404.
(61) Malard, L. M.; Pimenta, M. A.; Dresselhaus, G.; Dresselhaus, M. S. *Phys. Rep.* **2009**, *473*, 51−87.
(62) Nakano, Y.; Saeki, S.; Morikawa, T. *Appl. Phys. Lett.* **2009**, *94*, 22111.
(63) Gao, E.; Wang, W.; Shang, M.; Xu, J. *Phys. Chem. Chem. Phys.* **2011**, *13*, 2887−2893.
(64) Paracchino, A.; Brauer, J. C.; Moser, J. E.; Thimsen, E.; Graetzel, M. *J. Phys. Chem. C* **2012**, *116*, 7341−7350.
(65) Wang, L. C.; de Tacconi, N. R.; Chenthamarakshan, C. R.; Rajeshwar, K.; Tao, M. *Thin Solid Films* **2007**, *515*, 3090−3095.
(66) de Brito, J. F.; Araujo, A. R.; Rajeshwar, K.; Zanoni, M. V. B. *Chem. Eng. J.* **2015**, *264*, 302−309.
(67) Peter, L. M. *Chem. Rev.* **1990**, *90*, 753−769.
(68) Ma, Y.; Pendlebury, S. R.; Reynal, A.; Le Formal, F.; Durrant, J. R. *Chem. Sci.* **2014**, *5*, 2964.
(69) Klahr, B.; Gimenez, S.; Fabregat-Santiago, F.; Bisquert, J.; Hamann, T. W. *Energy Environ. Sci.* **2012**, *5*, 7626.
(70) Noack, V.; Weller, H.; Eychmuller, A. *J. Phys. Chem. B* **2002**, *106*, 8514−8523.
(71) Pu, Y. C.; Chou, H. Y.; Kuo, W. S.; Wei, K. H.; Hsu, Y. J. *Appl. Catal., B* **2017**, *204*, 21−32.
(72) Hansen, O.; Seger, B.; Vesborg, P. C. K.; Chorkendorff, I. *Science* **2015**, *350*, 1030−1031.



DOI: 10.1021/jacs.7b01820
*J. Am. Chem. Soc.* 2017, 139, 6682−6692